



Cite this: *J. Mater. Chem. A*, 2024, **12**, 33114

Structure–performance relationships of lithium-ion battery cathodes revealed by contrast-variation small-angle neutron scattering†

Qingsong Liu, ^{‡,a} Willa Brenneis, ^{‡,a} Gergely Nagy, ^b Mathieu Doucet, ^b Jeffrey Lopez ^{*,a} and Jeffrey J. Richards ^{*,a}

Lithium-ion battery cathodes are porous composites of active material, conductive carbon, and polymer binder. Controlling the cathode microstructure is key to achieving high energy density and cycling stability. Current characterization techniques lack the nanoscale resolution over representative volumes necessary to relate cathode microstructure to cycling performance. To address this challenge, we utilize contrast-variation small-angle neutron scattering to quantify the chemical and structural features of cathodes wet by dimethyl carbonate, representing a relevant solvent environment. Using neutron scattering measurements, we identify an expansion in carbon and polymer structures that arises after calendering and wetting with solvent. Further, we deconvolute the carbon and binder phases to obtain the solvent-accessible carbon black surface area, which we correlate to diminished capacity retention driven by electrolyte decomposition on exposed carbon. This technique provides nanoscale insight into composite cathode microstructures and resulting cycling performance, promising future applications to a broad range of porous materials that exist in energy storage systems.

Received 6th September 2024
Accepted 23rd October 2024

DOI: 10.1039/d4ta06364c
rsc.li/materials-a

Introduction

Lithium-ion batteries (LIBs) are crucial energy-storage systems that will facilitate the transition to a renewable, low-carbon future, reducing our reliance on fossil fuels.¹ Within the LIB, the composite cathode's microstructure controls the flow of ions and electrons and thus is a major driver of battery performance.^{2,3} To meet the energy density and rate capability targets necessary for accelerated electric vehicle adoption, the cathode microstructure must be engineered to achieve high ionic conductivity. The cathode microstructure consists of three phases: the active material (AM), carbon-binder domain (CBD), and pore space which is filled with an electrolyte during manufacturing. Significant effort has been devoted to optimizing the AM for stable, fast-charging cathodes,^{2–4} but a comprehensive understanding of the influence of the nanoscale CBD structure on cathode performance is lacking.

Though often considered a single phase, the carbon and binder within the CBD play distinct roles. Carbon creates

electronic pathways between the AM particles and the current collector.⁵ During slurry drying, the insulating binder coats the carbon to provide adhesion between the AM, carbon, and current collector.^{5,6} The binder then swells upon contact with the electrolyte, creating a distinction between the cathode microstructure in the wet and dry states.^{7,8} The composite CBD contains solvent-accessible nanopores (1–200 nm)^{9–11} which create circuitous ionic transport pathways that significantly increase cathode tortuosity.⁵ Techniques with sufficient resolution to identify these nanoscale features, such as transmission electron microscopy (TEM), are unable to measure the representative, micron-scale volumes needed to relate the overall nanostructure to cathode performance.¹² Tomography methods such as nano-computed tomography (nano-CT) and (plasma) focused ion beam scanning electron microscopy ((P)FIB-SEM) can resolve larger volumes, but overlook the influence of CB nanoporosity.^{9,10,12} Further, electron contrast (and thus SEM image contrast) from the binder and carbon are similar, necessitating the combination of these components into a single phase for analysis.^{12,13} (P)FIB-SEM has proven effective at providing an overview of the dry cathode structure,^{10,12} but is not yet possible to accomplish *in situ* when the cathode structure is wetted by an electrolyte. For an accurate understanding of the influence of the CBD on cathode performance, we must identify the distinct impacts of carbon and binder both in the wet state and at the nanoscale over a representative cathode volume.

Small-angle X-ray scattering (SAXS) and small-angle neutron scattering (SANS) are non-destructive techniques that offer

^aDepartment of Chemical and Biological Engineering, Northwestern University, Evanston, IL, USA, 60208. E-mail: jlopez@northwestern.edu; jeffrey.richards@northwestern.edu

^bNeutron Scattering Division, Oak Ridge National Laboratory, Oak Ridge, TN, 37831, USA

† Electronic supplementary information (ESI) available. See DOI: <https://doi.org/10.1039/d4ta06364c>

‡ Q. L. and W. B. contributed equally to this work.



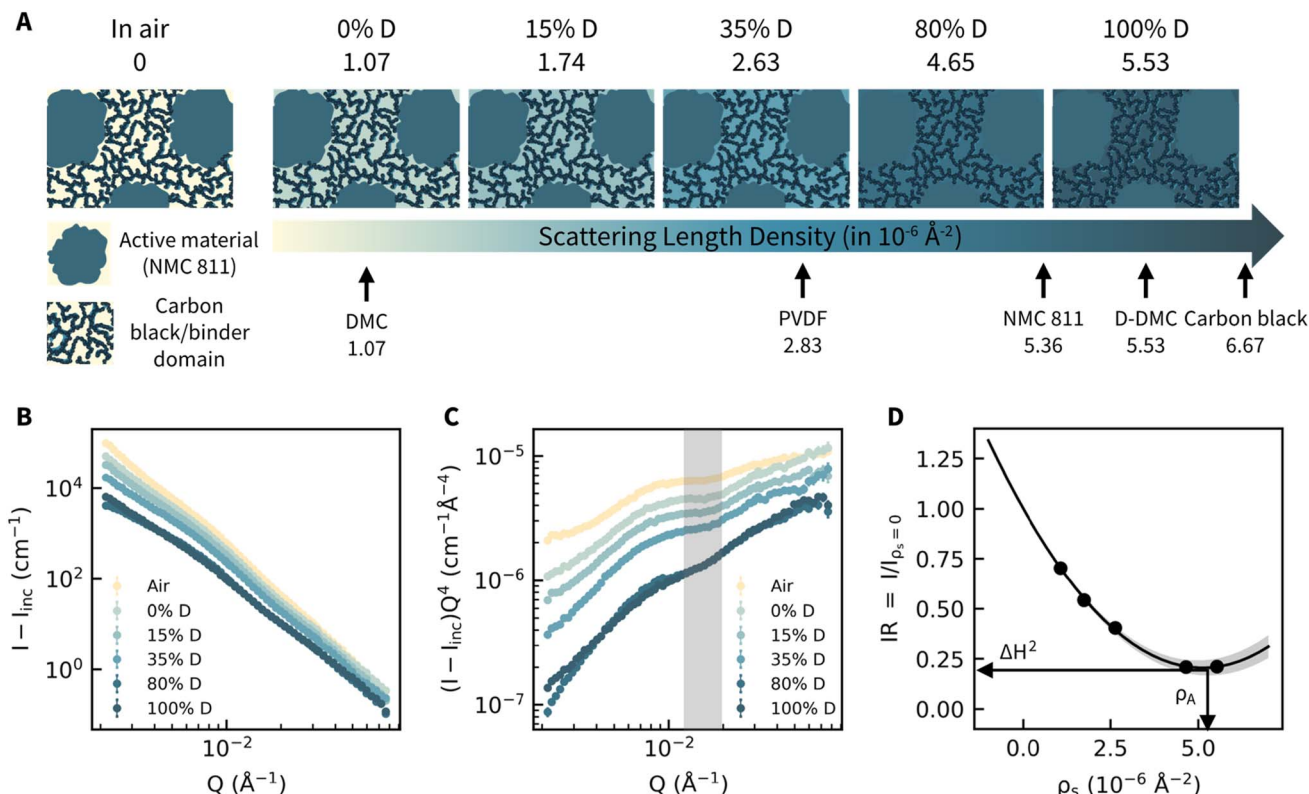


Fig. 1 CV-SANS measurements and limitations of general Porod's method analysis. (A) Illustration of the contrast variation series measurements. Scattering length density is calculated using the NIST neutron calculator and shown with the colormap. (B) Background (instrument and incoherent scattering) subtracted 1D scattering curves measured from the same electrode at different deuteration levels. (C) Porod's plots of the 1D scattering curves. The highlighted Q region corresponds to the length scale of the electrode/solvent interface, 31–52 nm. (D) Generalized Porod's scattering law analysis method.^{31,32} The Porod's constant at different ρ_s is approximated as the intensity at $Q = 0.0166 \text{ \AA}^{-1}$ due to the lack of Porod's regions at all contrasts. The obtained surface-averaged scattering length density, ρ_A , and the surface heterogeneity, ΔH^2 , are indicated.

multi-length scale (1–300 nm) structural information, making them well-suited for characterizing the porous structure of LIB cathodes at the nanoscale. Compared to SANS, SAXS has the advantage of high-flux, fast measurements which are suitable for *operando* studies. However, its application is usually limited to a single contrast and is much more sensitive to the heavier elements within the electrodes, thus neglecting the CBD. Detailed comparisons of SAXS and SANS can be found in several review papers.^{14–16} Previous studies employing SANS to investigate LIB systems focus on solid electrolyte interphase formation^{17,18} and lithiation mechanisms at the anode,^{19,20} and some only track the structural and chemical changes qualitatively.^{21,22} Quantitative analysis of composite cathode nanostructure requires a SANS method that can differentiate scattering contributions from individual components within the cathode. Contrast variation (CV), varying the amount of deuterium in the solvent wetting the pores of the electrode, is a generalized technique to achieve such analysis (Fig. 1A). CV-SANS has been leveraged to reveal valuable nanoscale structural insight by highlighting individual components within fuel cells and lithium–sulfur batteries.^{23–25} However, no previous studies have fully exploited the rich information intrinsically embedded in CV-SANS measurements to decouple the chemical and structural features.

In this work, we perform CV-SANS measurements on LIB cathodes and obtain scattering profiles from cathodes wetted by deuterium-substituted dimethyl carbonate (DMC), a common electrolyte solvent. From these scattering profiles, we extract quantitative structural and chemical information by calculating the basic functions²⁶ which describe the shape, the solvent penetration, and the solvated structure scattering in vacuum. We use this analysis to characterize electrodes manufactured with varying fabrication parameters, including a range of slurry solids loading and whether the cathode has been calendered. Leveraging the unique sensitivity of CV-SANS to the nanoscale features of the CBD, we use the basic functions to compare the wet and dry structures directly. Using this comparison, we show that calendered and uncalendered electrodes display distinct structural changes upon the addition of solvent. We find that at the nanoscale, the calendered electrode has a less dense carbon black agglomerate structure, and therefore a higher nanoscale porosity. This feature diverges from the decrease in apparent overall porosity after calendering. Using a physical model that extracts quantitative structural information from scattering parameters, we show that different processing conditions yield distinct structures. Relating structural information to electrochemical performance, we find that the amount of carbon black



exposed to solvent is strongly correlated to a decline in cycling performance, likely driven by electrolyte decomposition.

Results and discussion

Contrast variation small-angle neutron scattering (CV-SANS) measurements

We exploited CV-SANS to quantify the porous cathode structure by measuring a single uncalendered cathode immersed in DMC with varying levels of deuteration, displaying a range of scattering length density from $1.07 \times 10^{-6} \text{ \AA}^{-2}$ to $5.53 \times 10^{-6} \text{ \AA}^{-2}$, as shown in Fig. 1A. Scattering length density defines the scattering probability of a material, which depends on the material's density and composition. We also measured the dry cathode in air, for which scattering length density is approximate 0. We chose DMC because its hydrogenated/deuterated mixture solvents span the scattering length density of cathode components, which allows us to systematically explore the AM (active material, NMC811, $\text{LiNi}_{0.8}\text{Mn}_{0.1}\text{Co}_{0.1}\text{O}_2$), binder, (PVDF polyvinylidene difluoride, Arkema 761), and carbon black (CB, Super C65) within the cathode. DMC is commonly used as an electrolyte solvent²⁷ with similar surface tension and Hansen solubility parameters²⁸ as state-of-the-art electrolytes, indicating that the pore wetting within the electrode will be similar.^{29,30} In Fig. 1B, we obtained the background-subtracted scattering intensity from the cathode film as a function of the wave vector, Q , which is inversely proportional to the real-space distance at which scattering intensity originates. To identify the Q region where the solvent/electrode interface is probed, we construct a Porod's plot in Fig. 1C, plotted as IQ^4 vs. Q . For homogeneous and smooth interfaces, interfacial scattering should follow Porod's law,²⁶ which can be written as $I(Q) = C_P Q^{-4}$, where C_P is a constant that depends on the specific surface area and scattering length density of the solvent-accessible pore interfaces. In Fig. 1C, the lack of a plateau in the shaded region (length scale of 31–52 nm) at all solvent contrasts indicates complex interfaces within the composite, suggesting that no existing data analysis method is applicable to this system. SANS measurement of CB in *N*-methyl-2-pyrrolidone (NMP) shows a well-defined Porod's region (Fig. S1†) in the Q range of 0.012 to 0.019 \AA^{-1} . In this same Q range, measurements of AM particles also fulfill Porod's approximation (Fig. S2†). While the individual components' contributions fulfill Porod's approximation, the complex and non-homogenous interfaces in the electrode lead to non-zero power-law slopes in its Porod's plots.

While we apply the generalized CV-SANS method for data analysis, we first explore the application of the Generalized Porod's scattering law method (GPSLM),^{31,32} which proves to be inadequate for complex porous systems. The quadratic relation between the solvent scattering length density, ρ_s , and intensity ratio, $\text{IR} = C_P(\rho_s)/C_P(\rho_s = 0)$, shown in Fig. 1D, yields the surface averaged scattering length density, ρ_A , and the degree of heterogeneity, ΔH^2 , of the interfaces as discussed in ESI.3.† We expect there to be a distinction between dry and wet structures,³³ so we extrapolate to obtain $C_P(\rho_s = 0)$ rather than using the air measurement.²⁶ The finite value of $\Delta H^2 = 0.2$ confirms that the interfacial scattering at this length scale is

heterogeneous as the value of ΔH^2 ranges from 0, for chemically homogenous surface, to 1, for an extremely heterogeneous surface. The surface-averaged scattering length density ($\rho_A = 5.13 \times 10^{-6} \text{ \AA}^{-2}$), is intermediate to the scattering length density of each component, confirming that the interfacial scattering originates from a contribution of AM, CB, and PVDF.

While the GPSLM method seems to be a suitable method for capturing the interfacial information and could potentially address some of the issues present in complex heterogeneous porous structures³¹ (ESI.3†), this method has several limitations, and therefore new data analysis methods need to be developed to fully utilize the power of contrast variation measurements. First, the analysis shown in Fig. 1D uses the scattering intensity at a certain Q value rather than the fitted Porod's constant C_P because of the lack of Porod's region across contrasts, suggesting that the fitted parameters do not represent the quantitative information at the solvent/electrode interface. As indicated in Fig. 1C shaded region, the lack of Porod's region at a higher solvent deuteration level suggests structural inhomogeneity that GPSLM cannot resolve. In addition, GPSLM does not allow us to compare the wet and dry structures because the lowest solvent ρ_s ($1.07 \times 10^{-6} \text{ \AA}^{-2}$) is higher than the air ($\rho_{\text{air}} = 0 \text{ \AA}^{-2}$). This comparison is crucial to understanding the structural changes in electrochemically relevant environments. To resolve these issues, we build upon the contrast variation analysis first proposed by Sturmann^{26,34} for characterizing heterogeneous scattering from proteins and colloids in a dilute solution.

Decoupling structural and chemical features of CBD with the generalized contrast variation method

For any binary system comprised of a solid and a solvent phase, the scattering intensity can be decomposed as

$$I(Q, \rho_s) = \rho_s^2 I_1(Q) - 2\rho_s I_{01}(Q) + I_0(Q) \quad (1)$$

$I_0(Q)$, $I_{01}(Q)$, and $I_1(Q)$ are called the basic functions which depend on the solvent penetration (ϕ_s) and scattering length density of the solid phase within the measured sample. Mathematical definitions of each basic function are given in ESI.4.† ϕ_s is defined as the volume that can be accessed by the solvent, and therefore any internal solvent-inaccessible pores within solids are mathematically defined as part of the solid phase in this analysis. While solvent-inaccessible pores exist within NMC 811 particles,³⁵ they are considered part of solid inhomogeneity and do not contribute to solvent-dependent scattering intensity. $I_1(Q)$ is the scattering of the solid phase without considering the scattering length density, and therefore is only dependent on the shape of the solid phase. The functional form of $I_0(Q)$ is the complete sum of contrast-dependent two-point correlation, which is equivalent to the scattering of the solvated solid phase at $\rho_s = 0 \text{ \AA}^{-2}$. $I_{01}(Q)$ is the cross-term that is necessary to account for solvent penetration. The functional form of $I(Q, \rho_s)$ implies that the total intensity of a contrast variation series will follow a quadratic pattern and by fitting the scattering intensity across the contrast variation series at different Q , we can determine the basic functions. In Fig. 2, we show the illustration of the basic



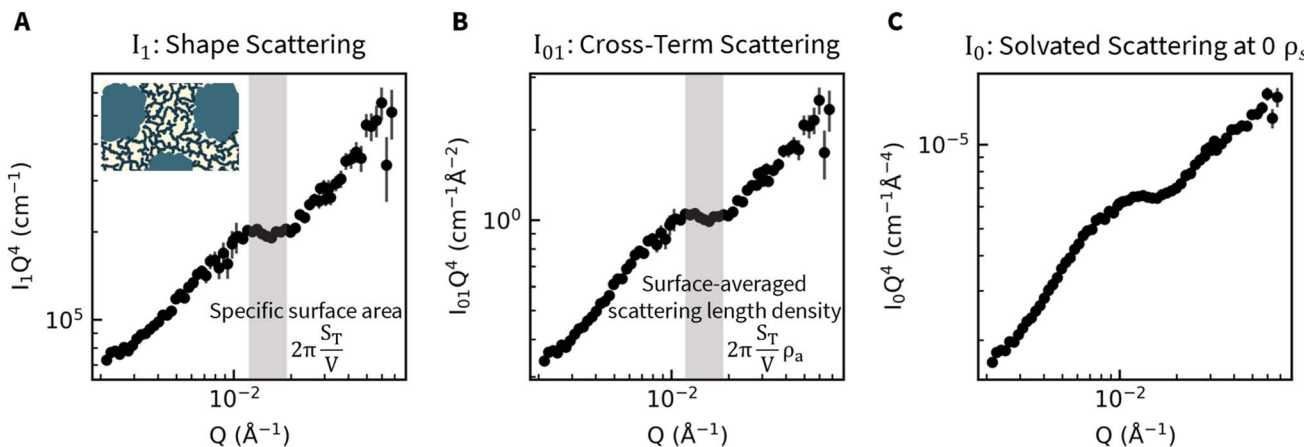


Fig. 2 Generalized contrast variation method and the obtained basic functions for decoupled structural and chemical characterization. (A). Illustration and Porod's plot of basic function $I_1(Q)$. $I_1(Q)$ represents the shape scattering of the electrode without being weighted by the scattering length density. The obtained $\frac{S_T}{V}$ value is $3.15 \text{ m}^2 \text{ cm}^{-3}$ (B). Porod's plot of basic function $I_{01}(Q)$. $I_{01}(Q)$ represents the cross-term scattering of the electrode which is weighted by the scattering length density once. The obtained ρ_A value is $5.18 \times 10^{-6} \text{ \AA}^{-2}$. (C). Porod's plot of basic function $I_0(Q)$ which represents the solvated structure scattering at 0 solvent scattering length density.

functions obtained by fitting the SANS data from Fig. 1. In Fig. 2A, $I_1(Q)$ represents the shape of the solid phase at infinite contrast where internal variations of the solid phase scattering length density do not contribute to the scattering. $I_1(Q)$ unambiguously shows a Porod's region in the previously identified Q region. Due to the absence of the scattering length density in the mathematical definition in $I_1(Q)$, I_1Q^4 obtained in the shaded region is equal to the specific surface area by volume, $2\pi S_T/V$, of the solid phase that is solvent-accessible. To obtain ρ_A , the surface averaged scattering length density, we can simply calculate the ratio, $\langle I_{01}Q^4 \rangle / \langle I_1Q^4 \rangle$, in the same Q region of interest, as highlighted in Fig. 2B. In Fig. 2C, we also show I_0Q^4 , the scattering of the wet electrode at 0 solvent ρ_s , which allows us to obtain previously inaccessible SANS information. As discussed in ESI.5,† this CV-SANS method using basic functions can be rearranged into the Sturmann method (for the radius of gyration) and the GPLSM (for surface characterization) but fully exploits the rich information embedded in the CV-SANS measurements.

Qualitative structural differences of electrodes manufactured with various processing conditions

To probe the nanoscale structural changes induced by the addition of solvent, we show the direct comparison of the wet ($I_0(Q)$) and dry ($I_{\text{air}}(Q)$) structure for the uncalendered cathode in Fig. 3A. Qualitative differences emerge at two length scales, $<10 \text{ nm}$ and $>160 \text{ nm}$. The addition of DMC induces swelling in the polymer phase,³⁶ allowing us to attribute this difference at $<10 \text{ nm}$ to the swelling of polymer chains. The swollen polymer results in a power law scaling change in $I(Q)$ and Porod's plot. We can also assign the origin of the difference at $>160 \text{ nm}$ to polymer swelling. Considering that PVDF coats the CB surface, the swelling of PVDF can decrease the compactness of the CB agglomerates, resulting in a stronger power law scaling in Porod's plot. This hypothesis is further supported by the observation that for SANS measurements above this length

scale, scattering intensity comes from the CB agglomerate structure (Fig. S1D†).³⁷⁻³⁹ In the case of calendered film (Fig. 3B), we only observe structural changes at the smaller length scale. This trend suggests that upon the addition of solvent in the calendered film, while PVDF chains are still swollen, the CB agglomerate fractal dimension, or the compactness of the agglomerate, remains unchanged. This observation can be explained by the decreased plastic deformability of the electrode matrix⁴⁰⁻⁴⁵ resulting from the calendering process, which leads to a more rigid structure that is less prone to structural changes upon solvent addition.

To further probe structural changes induced by the calendering process, we conducted CV-SANS measurements on 12 electrodes manufactured from different processing conditions (SANS parameters presented in Table S1†). We varied the solid content in the slurry state (38, 42, and 46 wt%) and the effective coating shear rate (874.9 and 13.1 s^{-1}).

In Fig. 3C, we present the normalized dry structure I_{air} Porod's plots. Regardless of the coating shear rate or the slurry solid content, we can classify electrodes based on the calendering process. In the low Q region, calendered electrodes' Porod's plots indicate a smaller CB fractal dimension and more open CB agglomerates. This suggests that while the calendering process reduces the overall electrode porosity (Table S2†), CB agglomerates become more open at the nanoscale due to the external stress experienced during the calendering process. The manifestation of this phenomenon ubiquitously exists in porosimetry data⁴⁵⁻⁴⁸ where the volume of the nanopores ($<100 \text{ nm}$) increases significantly with an increasing degree of calendering even before AM particles show any internal cracking. Here, we show that the origin of this previously unexplained phenomenon is the direct result of a more open CB agglomerate nanoscale structure, further supported by our porosimetry measurements (ESI.6, Fig. S3†). While it is known that breakup of agglomerates is mediated in suspensions by hydrodynamic forces,^{37,49,50} observations from both the SANS and porosimetry measurements



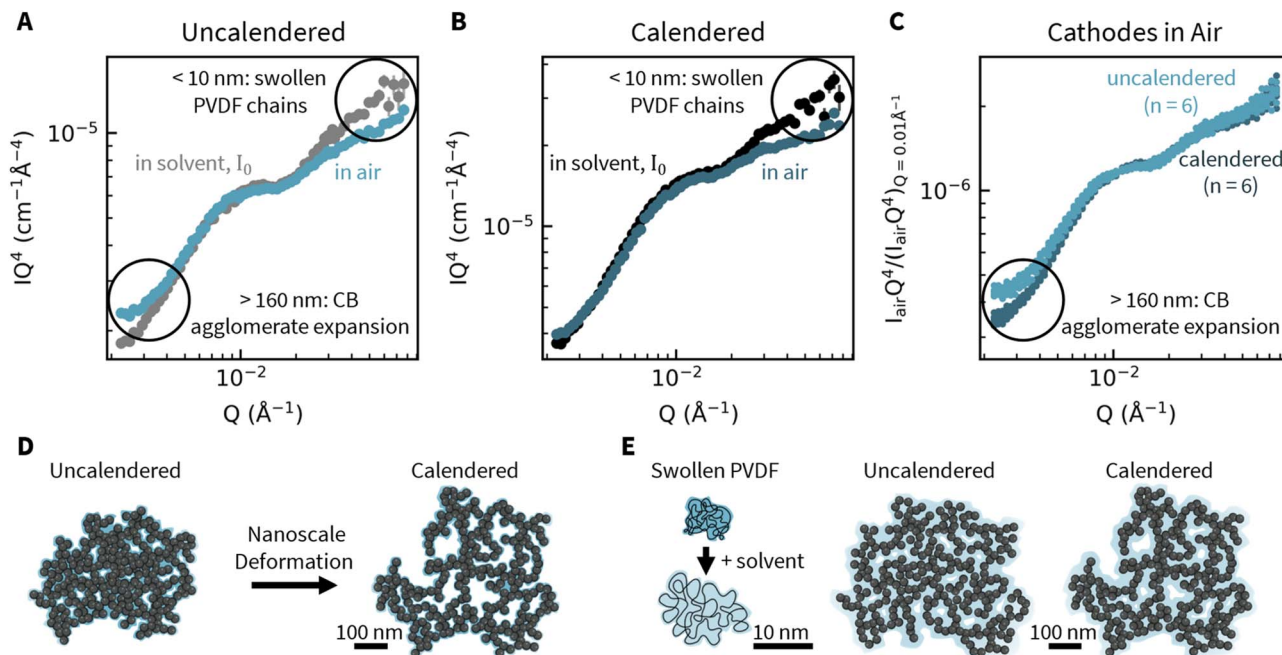


Fig. 3 Nanoscale structure changes of electrodes probed by SANS measurements. (A) Porod's plots of uncalendered film's dry and wet structures. Structural differences are observed at two length scales and circled in the plots. The length scales are <10 nm and >160 nm. (B) Porod's plots of calendered film's dry and wet structures. Structural differences are observed at only one length scale: <10 nm. (C) Normalized dry structures of 12 electrodes processed with various conditions (solid content, coating speed, and the calendering process). Calendered films show consistent deviations from uncalendered films due to a more open CB agglomerate structure. (D) Illustration of the nanoscale carbon/binder domain changes induced by the calendering process and (E) The addition of solvent.

suggest a similar behavior in solid-phase deformation imposed by calendering. An illustration of the calendering process and the polymer swelling behavior in both calendered and uncalendered samples is presented in Fig. 3D and E.

Structure–performance relationships of LIB cathodes

We evaluated the electrochemical cycling performance for each cathode in half cells with Li metal counter electrodes and 1.2 M lithium hexafluorophosphate (LiPF_6) in ethylene carbonate (EC) and ethyl methyl carbonate (EMC) (3 : 7 w/w) as the electrolyte (Fig. 4A). Each data point represents the average discharge capacity of three replicate cells constructed with electrodes from the same sheet. Error bars indicate one standard deviation. We quantify distinctions between fabricated electrodes using a simple model (Fig. 4B) that uses SANS parameters to solve for relevant cathode microstructural properties including PVDF coverage rate (χ), (*i.e.* the fraction of carbon surface that is coated with PVDF), PVDF layer thickness (ξ), and the percentage CB surface area (θ) that is not lost due to dense agglomeration and is still accessible to solvent and PVDF. The detailed construction of the model is presented in ESI.7.† We also assume that both the AM and CBD lose 10% of their surface area due to contact, accounting for contact between the CB and AM as well as between the PVDF and AM (ESI.8†).⁵¹ This assumption allows us to solve the model presented in Fig. 4B and identify the disparate influences of each component within the CBD, for the first time deconvoluting the influence of CB and PVDF.

Eqn (2) states that the sum of all species' surface area at the interface equates to the solvent-accessible surface area from $I_1(Q)$,

$$S_T = S_{\text{CB}} + S_{\text{AM}} + S_{\text{PVDF}} \quad (2)$$

and eqn (3) constrains the amount of each species that is present at the interface through the surface-area weighted scattering length density obtained from $I_{01}(Q)$,

$$S_T(\rho) = S_{\text{CB}}\rho_{\text{CB}} + S_{\text{AM}}\rho_{\text{AM}} + S_{\text{PVDF}}\rho_{\text{PVDF}}. \quad (3)$$

In addition, eqn (4) represents the mass conservation of PVDF within the electrode, where N_{CB} is the number of CB particles per gram of cathode calculated from the mass balance (ESI.7†), R_{CB} the radius of the CB primary particle, and ξ is the PVDF layer thickness,

$$V_{\text{PVDF}} = \frac{4\pi}{3} \chi \theta N_{\text{CB}} \left((R_{\text{CB}} + \xi)^3 - (R_{\text{CB}})^3 \right). \quad (4)$$

The SANS-based structural parameters for each cathode condition are presented in Table 1. The broad variation in scattering-based structural characteristics across cathode coating conditions demonstrates that different fabrication processes lead to varying cathode microstructures. We find an excellent correlation between electrochemical impedance spectroscopy (EIS) based surface capacitance and SANS-based CB surface area, along with good agreement of derived CB



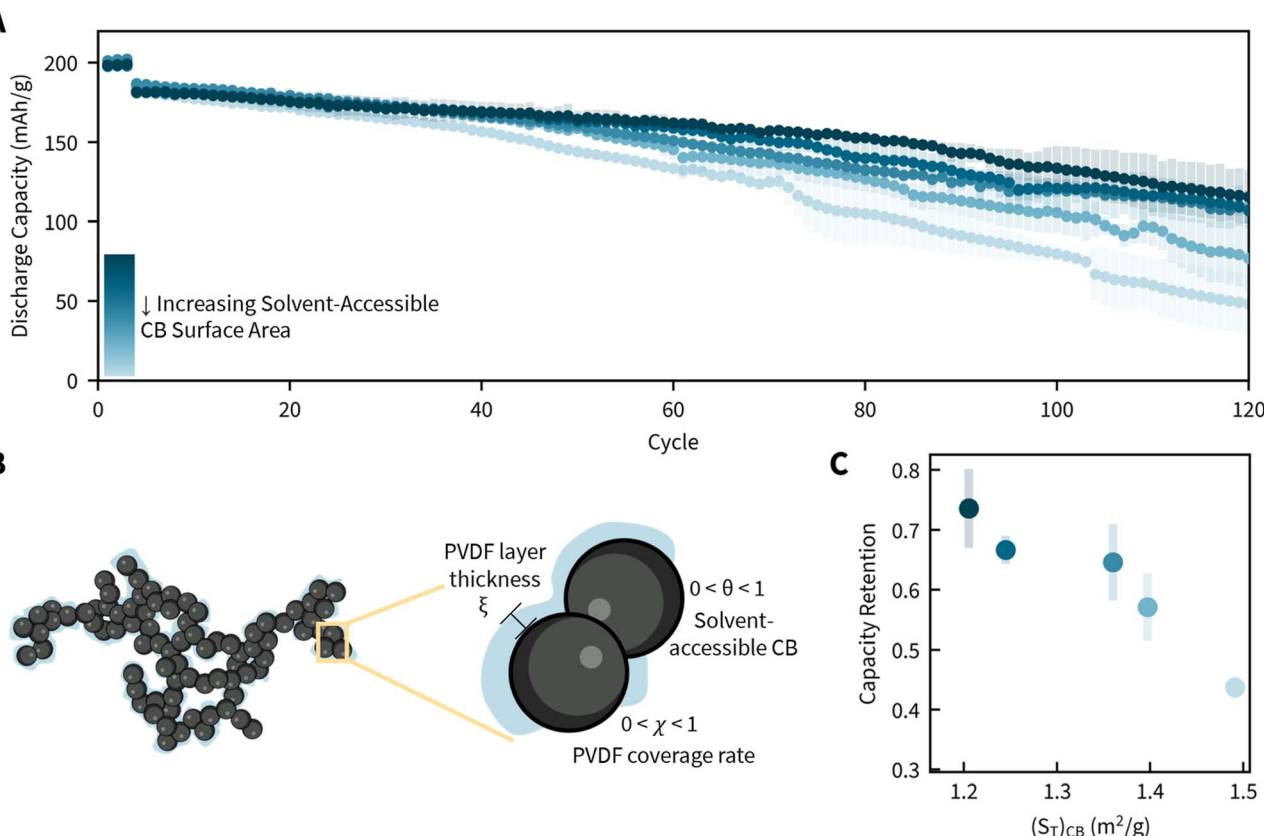


Fig. 4 Structure–performance relationships of LIB cathodes. (A) Cycling performance at C/3 (1C = 190 mA h g^{−1}) across manufacturing conditions. The color gradient is aligned with the degree of exposed CB surface area. (B) A physical model that extracts structural parameters from scattering parameters. In this model, key structural parameters account for CB agglomeration and PVDF covering the surface of CB. (C) Discharge capacity retention after 100 cycles at C/3 and SANS-based carbon black surface area. Increased solvent-accessible carbon black surface area results in a decline in long-term discharge capacity.

Table 1 Scattering-based structural parameters across cathode coating conditions

		Slurry solids content	Surface area (m ² g ^{−1})	CB surface retention (θ)	PVDF coverage rate (χ)	PVDF layer thickness (ξ , nm)	CB fractional surface (m ² g ^{−1})	PVDF fractional surface (m ² g ^{−1})
Calendered	High shear	38	1.59	0.425	0.314	22.552	1.205	0.278
		42	2.24	0.626	0.475	13.613	1.360	0.776
		46	1.44	0.371	0.230	29.089	1.179	0.154
	Low shear	38	1.46	0.367	0.179	33.472	1.245	0.108
		42	1.84	0.493	0.314	20.656	1.397	0.338
		46	1.88	0.496	0.273	22.383	1.489	0.284
Uncalendered	High shear	38	1.18	0.284	0.125	45.736	1.026	0.045
		42	2.01	0.564	0.475	14.583	1.224	0.682
		46	1.43	0.371	0.246	28.030	1.155	0.168
	Low shear	38	1.42	0.339	0.085	50.401	1.279	0.034
		42	1.72	0.460	0.314	21.525	1.306	0.309
		46	1.65	0.434	0.271	24.292	1.308	0.236

capacitance with literature,⁵² lending confidence to our model (ESI.9, Fig. S8†). From this model, we can uniquely deconvolute the influence of CB and PVDF within the CBD, both at the nanoscale and over the entire cathode volume.

We directly relate structural parameters to electrochemical performance in Fig. 4C, showing that electrodes with more solvent-accessible carbon black surface area as measured by

SANS retain less capacity after 100 cycles, likely due to electrolyte decomposition. We calculate capacity retention by comparing the discharge capacity of the first C/3 cycle to the 100th cycle and observe this trend across different cycle numbers ranging from 40 to 100 (Fig. S5†). CB is known to catalyze electrolyte decomposition⁵³ and increased CB surface area provides more sites for the decomposition to occur.^{54,55}

Furthermore, CB is populated with oxygen-containing functional groups,⁵³ which can oxidize LiPF₆ and carbonate-containing electrolytes to form lithium alkyl carbonate-based decomposition products.^{56,57} Electrolyte oxidation results in the growth of a passivation layer on the CB surface⁵⁸ and can contribute to the propagation of the cathode-electrolyte interphase on the AM.⁵⁷ Electrolyte decomposition and interphase growth reduce electronic conductivity, increase interfacial resistance between the conductive carbon and active material particles, and contribute to a loss in coulombic efficiency during cycling.⁵⁴ We demonstrate here that electrode manufacturing parameters are critical in controlling the cathode microstructure, including exposed CB surface area, and advancing cycling performance. SANS is a uniquely well-equipped tool to understand nanoscale distinctions in composite cathode structure and has allowed us to isolate each component and draw clear connections between cathode structure and cycling performance.

Conclusions

In summary, we utilize CV-SANS to decouple the nanoscale chemical and structural features of porous LIB cathodes *in situ*. We analyze a large cathode volume at nanoscale resolution, enabling a representative understanding of the cathode microstructure that is lacking in common tomography techniques. Our CV-SANS analysis extends beyond the existing applications of Sturmann's method to obtain three basic functions that describe the shape, the solvent penetration, and the solvated structure at 0 scattering length density of the porous cathodes. The solvated structure functions of electrodes at 0 scattering length density enables direct comparison between the dry and wet electrode structures. The binder swells upon the addition of the solvent, a phenomenon identified in previous studies.^{7,8} However, the application of CV-SANS enables us to uniquely uncover the impact of this swelling on nanoscale porosity and CBD structure. Further, we contrast the impact of this swelling on CB agglomerates across calendered and uncalendered samples. In uncalendered samples, the binder swelling induces a more open CB agglomerate structure. This behavior is not observed in calendered samples, as calendering results in a more rigid structure and prevents the swelled binder from forcing CB agglomerates to expand. We further show that at the nanoscale, the calendering process creates a more open CB agglomerate structure in the dry cathodes by imposing external stress, in sharp contrast to the reduced nominal porosity. This phenomenon has been presented without discussion in porosimetry data,^{47,48} but here we are able to explain its origin, highlighting the importance of nanoscale characterization.

With the shape and the solvent penetration scattering functions, we obtain the specific surface area and the average scattering length density of the pores that are accessible to the solvent. By constructing a model that utilizes scattering parameters, we extract important structural parameters that allow us to quantitatively calculate the amount of carbon and binder present at the cathode/solvent interface. Upon electrochemical evaluation of calendered electrodes with varying

processing conditions, we find a strong correlation between the CB surface exposed to the electrolyte and capacity fade during cycling, which can be attributed to exposed CB catalyzing electrolyte oxidation. While previous publications attribute carbon black surface to a decline in battery performance,^{53,54,56–58} we use CV-SANS to quantify this effect across cathode processing conditions with a level of detail previously inaccessible. Crucially, we use a single technique to draw multiple conclusions about the nature of the cathode microstructure at the nanoscale, *in situ*, and over a representative volume.

The generalized CV-SANS method will greatly expand the toolkit for analyzing CV-SANS measurements. We show that in addition to special cases such as the surface scattering and radius of gyration, scattering at any *Q* values or length scales can be decomposed to describe the structure and chemical information individually without any assumptions. We further show that while for most organic solvents it is impossible to experimentally measure the wet structure at 0 scattering length density, this method provides a quantitative and reliable extrapolation to such a condition, which enables a direct comparison between the wet and dry nanostructures.

We anticipate that further *operando* measurements on porous electrodes using this method will reveal the nanoscale evolution of the interfaces during cycling to better understand interphase formation and evolution, secondary particle fracture, and changes in interfacial fraction of electrode components for materials with large structural changes such as alloy and conversion electrodes. Most importantly, because our generalized CV-SANS method has no assumptions on the nature of the systems, it has the potential to be used to systematically evaluate the contrast variation scattering profiles of any heterogeneous samples that are present ubiquitously in the chemical, biological, and materials sciences.

Materials and methods

Electrode & coin cell fabrication, cell cycling

Composite electrodes were fabricated in a 90:5:5 ratio (by weight) of LiNi_{0.8}Mn_{0.1}Co_{0.1}O₂ (NMC811, MSE Supplies), polyvinylidene fluoride (PVDF, Arkema, 761), and Super C65 conductive carbon black (MSE Supplies). To control the slurry solid content, the PVDF was first dissolved in *N*-methyl-2-pyrrolidone (NMP, Fisher) in weight fractions of 3–4%. Half of the PVDF:NMP solution was then added to the NMC811 and carbon black and mixed in a planetary mixer (Thinky, AR-100) for 7 minutes at 2000 rpm. The second half of the PVDF:NMP solution was then added to the slurry, which was mixed in the planetary mixer for 12 minutes at 2000 rpm.

Slurries were coated onto a 25.4 µm thick aluminum current collector (Grainger) using a blade coater (BYK, byko-drive S) with a gap height of 254 µm. The speed of the blade was set to 3 mm s⁻¹ or 200 mm s⁻¹ for the low or high shear conditions, respectively. The coated electrodes were dried under vacuum at 60 °C for 1 hour followed by 12 hours in a fume hood. The electrodes were then punched into 12 mm discs. While different calendering parameters could lead to different cathode structures,⁵⁹ consistent calendering parameters were used (including



roll gap height, roll speed, and roll temperature) in our experiments. The calendered samples were sandwiched between stainless steel shims and calendered with a roll press (TOB, JS-200L) at room temperature with a roll gap of 0.1 mm. The areal capacity and mass loading varied based on slurry formulation and coating speed and are tabulated in Table S3.† Electrodes were dried under a vacuum overnight before being assembled into half cells.

Lithium||composite cathode half cells were prepared in a glovebox ($O_2 < 0.5$ ppm, $H_2O < 0.1$ ppm) using 60 μ L of electrolyte (1.2 M lithium hexafluorophosphate (LiPF₆, MSE) in ethylene carbonate (EC, Gotion) and ethyl methyl carbonate (EMC, Gotion) (3 : 7 w/w)). Lithium foil with 500 μ m thickness (MSE Supplies) was punched into 15 mm discs. CR2032 coin cells (MTI Corp.) with Celgard 2325 separators were assembled to evaluate the electrochemical performance of the cathodes. A theoretical capacity of 190 mA h g⁻¹ for NMC811 was used for all C rate calculations. C-rate refers to the charge/discharge rate applied to the cells. 1C indicates that current is applied such that each charge takes one hour, and C/3 indicates that each charge takes three hours. Long-term cycling was conducted on an Arbin battery cycler at room temperature with a voltage window of 3 V to 4.3 V with three constant-current, constant voltage (CC-CV) formation cycles at C/10 followed by cycling at C/3.

Small-angle neutron scattering (SANS) measurements

SANS measurements were performed on the Extended Q-range Small-Angle Neutron Scattering Diffractometer at the Spallation Neutron Source of the Oak Ridge National Lab (Oak Ridge, TN).^{60,61} Three configurations were utilized to access the entire Q range from 0.0019 to 0.2675 Å⁻¹, where $Q = \frac{4\pi}{\lambda} \sin\left(\frac{\theta}{2}\right)$. λ is the neutron wavelength and θ is the scattered angle. The neutron wavelength band and the detector distance for the three configurations are 15–17.9 Å/9 m, 7–10.6 Å/4 m, and 2.5 – 6.1 Å/4 m, which theoretically covered the Q range from 0.0023 to 0.0343 Å⁻¹, 0.0074 to 0.1672 Å⁻¹, and 0.0174 to 0.356 Å⁻¹ respectively. Data acquired from three configurations were first reduced by using the drtsan software⁶² {Heller, 2022 #168} and then merged in the Q range from 0.0097 to 0.0107 Å⁻¹ and 0.028 to 0.033 Å⁻¹. The final Q range is 0.002 to 0.356 Å⁻¹.

All measurements were conducted using standard demountable cells with a path length of 0.5 mm. For each processing condition, contrast variation series were performed on the same electrode. SANS measurements of electrodes in air were performed first, followed by SANS measurements in dimethyl carbonate (DMC) of different deuteration levels. Before each solvent exchange step, the radioactivity team cleared the samples by ensuring that the radioactivity was within the safety limit. The demountable cells were then disassembled in a fume hood where the samples were left to be dried for 5 minutes, which is sufficient to dry a small quantity (~5 μ L) of highly evaporative solvent DMC over a large area (0.177 cm²). The scattering length density of materials was calculated using the Neutron

Activation and Scattering Calculator (<https://www.ncnr.nist.gov/resources/activation/>).

Abbreviations

SANS	Small-angle neutron scattering
CV	Contrast variation
AM	Active material
CB	Carbon black
PVDF	Polyvinylidene difluoride
CBD	Carbon-binder domain
TEM	Transmission electron microscopy
SEM	Scanning electron microscopy
(P)FIB-SEM	(Plasma) focused ion beam scanning electron microscopy
Nano-CT	Nano-computed tomography
DMC	Dimethyl carbonate
GPSLM	Generalized Porod's scattering law method

Data availability

The data supporting this article have been included as part of the ESI.† The raw data for this article, including small-angle neutron scattering, battery half-cell cycling, and blocking electrolyte impedance spectroscopy, are available at Northwestern University Data Repository at <https://doi.org/10.21985/n2-q9b6-z794>.

Conflicts of interest

There are no conflicts to declare.

Acknowledgements

This material was based upon work supported by the U.S. Department of Energy, Office of Science, Office of Basic Energy Sciences, under Award No. DE-SC-0022119. A portion of this research used resources at the Spallation Neutron Source, a DOE Office of Science User Facility operated by the Oak Ridge National Laboratory. The beam time was allocated to BL-6, EQ-SANS, on proposal number IPTS-30638. Q. L. acknowledged that this research was supported in part by an appointment to the Oak Ridge National Laboratory GRO Program, sponsored by the U.S. Department of Energy and administered by the Oak Ridge Institute for Science and Education. Q. L. gratefully acknowledges support from the Ryan Fellowship and the International Institute for Nanotechnology at Northwestern University. W. B. gratefully acknowledges support by the National Science Foundation Graduate Research Fellowship Program (NSF-GRFP). This work made use of the EPIC facility of Northwestern University's NUANCE Center, which has received support from the SHyNE Resource (NSF ECCS-2025633), the IIN, and Northwestern's MRSEC program (NSF DMR-2308691). This research used resources of the Advanced Photon Source, a U.S. Department of Energy (DOE) Office of Science user facility operated for the DOE Office of Science by Argonne National Laboratory under Contract No. DE-AC02-06CH11357.



Notes and references

1 B. Diouf and R. Pode, Potential of Lithium-Ion Batteries in Renewable Energy, *Renewable Energy*, 2015, 375–380, DOI: [10.1016/j.renene.2014.11.058](https://doi.org/10.1016/j.renene.2014.11.058).

2 R. Ge, A. M. Boyce, Y. Sun, P. R. Shearing, P. S. Grant, D. J. Cumming and R. M. Smith, Numerical Design of Microporous Carbon Binder Domains Phase in Composite Cathodes for Lithium-Ion Batteries, *ACS Appl. Mater. Interfaces*, 2023, 15(23), 27809–27820, DOI: [10.1021/acsami.3c00998](https://doi.org/10.1021/acsami.3c00998).

3 J. E. Vogel, M. M. Forouzan, E. E. Hardy, S. T. Crawford, D. R. Wheeler and B. A. Mazzeo, Electrode Microstructure Controls Localized Electronic Impedance in Li-Ion Batteries, *Electrochim. Acta*, 2019, 297, 820–825, DOI: [10.1016/j.electacta.2018.11.204](https://doi.org/10.1016/j.electacta.2018.11.204).

4 S. Hein, T. Danner, D. Westhoff, B. Prifling, R. Scurtu, L. Kremer, A. Hoffmann, A. Hilger, M. Osenberg, I. Manke, M. Wohlfahrt-Mehrens, V. Schmidt and A. Latz, Influence of Conductive Additives and Binder on the Impedance of Lithium-Ion Battery Electrodes: Effect of Morphology, *J. Electrochem. Soc.*, 2020, 167(1), 013546, DOI: [10.1149/1945-7111/ab6b1d](https://doi.org/10.1149/1945-7111/ab6b1d).

5 J. Entwistle, R. Ge, K. Pardikar, R. Smith and D. Cumming, Carbon Binder Domain Networks and Electrical Conductivity in Lithium-Ion Battery Electrodes: A Critical Review, *Renewable Sustainable Energy Rev.*, 2022, 112624, DOI: [10.1016/j.rser.2022.112624](https://doi.org/10.1016/j.rser.2022.112624).

6 W. Bauer and D. Nötzel, Rheological properties and stability of NMP based cathode slurries for lithium ion batteries, *Ceram. Int.*, 2014, 40, 4591–4598.

7 S. Byun, Y. Roh, K. M. Kim, M. H. Ryou and Y. M. Lee, Toward Understanding the Real Mechanical Robustness of Composite Electrode Impregnated with a Liquid Electrolyte, *Appl. Mater. Today*, 2020, 21, 100809, DOI: [10.1016/j.apmt.2020.100809](https://doi.org/10.1016/j.apmt.2020.100809).

8 J. Qian, C. G. Wiener, Y. Zhu and B. D. Vogt, Swelling and Plasticization of Polymeric Binders by Li-Containing Carbonate Electrolytes Using Quartz Crystal Microbalance with Dissipation, *Polymer (Guildf)*, 2018, 143, 237–244, DOI: [10.1016/j.polymer.2018.04.021](https://doi.org/10.1016/j.polymer.2018.04.021).

9 S. R. Daemi, C. Tan, T. Volkenandt, S. J. Cooper, A. Palacios-Padros, J. Cookson, D. J. L. Brett and P. R. Shearing, Visualizing the Carbon Binder Phase of Battery Electrodes in Three Dimensions, *ACS Appl. Energy Mater.*, 2018, 1(8), 3702–3710, DOI: [10.1021/acsaeem.8b00501](https://doi.org/10.1021/acsaeem.8b00501).

10 S. Vierrath, L. Zielke, R. Moroni, A. Mondon, D. R. Wheeler, R. Zengerle and S. Thiele, Morphology of Nanoporous Carbon-Binder Domains in Li-Ion Batteries - A FIB-SEM Study, *Electrochem. Commun.*, 2015, 60, 176–179, DOI: [10.1016/j.elecom.2015.09.010](https://doi.org/10.1016/j.elecom.2015.09.010).

11 S. Ban, K. Malek, C. Huang and Z. Liu, A molecular model for carbon black primary particles with internal nanoporosity, *Carbon (NY)*, 2011, 49, 3362–3370.

12 M. Zhang, M. Chouchane, S. A. Shojaee, B. Winiarski, Z. Liu, L. Li, R. Pelapur, A. Shodiev, W. Yao, J. M. Doux, S. Wang, Y. Li, C. Liu, H. Lemmens, A. A. Franco and Y. S. Meng, Coupling of Multiscale Imaging Analysis and Computational Modeling for Understanding Thick Cathode Degradation Mechanisms, *Joule*, 2023, 7(1), 201–220, DOI: [10.1016/j.joule.2022.12.001](https://doi.org/10.1016/j.joule.2022.12.001).

13 B. Song, T. Sui, S. Ying, L. Li, L. Lu and A. M. Korsunsky, Nano-Structural Changes in Li-Ion Battery Cathodes during Cycling Revealed by FIB-SEM Serial Sectioning Tomography, *J. Mater. Chem. A*, 2015, 3(35), 18171–18179, DOI: [10.1039/c5ta04151a](https://doi.org/10.1039/c5ta04151a).

14 H. Zhu, Y. Huang, H. Zhu, L. Wang, S. Lan, X. Xia and Q. Liu, In Situ Probing Multiple-Scale Structures of Energy Materials for Li-Ion Batteries, *Small Methods*, 2020, 1900223, DOI: [10.1002/smtd.201900223](https://doi.org/10.1002/smtd.201900223).

15 Y. Ren and X. Zuo, Synchrotron X-Ray and Neutron Diffraction, Total Scattering, and Small-Angle Scattering Techniques for Rechargeable Battery Research, *Small Methods*, 2018, 2(8), 1800064, DOI: [10.1002/smtd.201800064](https://doi.org/10.1002/smtd.201800064).

16 L. Fang, R. E. Winans and T. Li, Synchrotron small-angle X-ray scattering technique for battery electrode study, *Nano Energy*, 2024, 121, 109255.

17 R. L. Sacci, *et al.*, Structure of spontaneously formed solid-electrolyte interphase on lithiated graphite determined using small-angle neutron scattering, *J. Phys. Chem. C*, 2015, 119, 9816–9823.

18 C. A. Bridges, X. G. Sun, J. Zhao, M. P. Paranthaman and S. Dai, In situ observation of solid electrolyte interphase formation in ordered mesoporous hard carbon by small-angle neutron scattering, *J. Phys. Chem. C*, 2012, 116, 7701–7711.

19 C. J. Jafta, *et al.*, Probing microstructure and electrolyte concentration dependent cell chemistry via operando small angle neutron scattering, *Energy Environ. Sci.*, 2019, 12, 1866–1877.

20 J. Hattendorff, S. Seidlmayer, H. A. Gasteiger and R. Gilles, Li-ion half-cells studied operando during cycling by small-angle neutron scattering, *J. Appl. Crystallogr.*, 2020, 53, 210–221.

21 S. Seidlmayer, *et al.*, Operando Small-Angle Neutron Scattering (SANS) on Li-Ion Batteries, *J. Electrochem. Soc.*, 2015, 162, A3116–A3125.

22 C. J. Jafta, *et al.*, Probing the Li₄Ti₅O₁₂ Interface Upon Lithium Uptake by Operando Small Angle Neutron Scattering, *ChemSusChem*, 2020, 13, 3654–3661.

23 F. Chabot, *et al.*, Detailed Catalyst Layer Structure of Proton Exchange Membrane Fuel Cells from Contrast Variation Small-Angle Neutron Scattering, *ACS Appl. Energy Mater.*, 2023, 6, 1185–1196.

24 Y. C. Chien, M. J. Lacey, N. J. Steinke, D. Brandell and A. R. Rennie, Correlations between precipitation reactions and electrochemical performance of lithium-sulfur batteries probed by operando scattering techniques, *Chem*, 2022, 8, 1476–1492.

25 S. Risse, E. Häck, B. Kent and M. Ballauff, Operando Analysis of a Lithium/Sulfur Battery by Small-Angle Neutron Scattering, *ACS Nano*, 2019, 13, 10233–10241.



26 L. A. Feigin and D. I. Svergun, *Structure Analysis by Small-Angle X-Ray and Neutron Scattering*, Springer, USA, 2013.

27 K. Xu, Nonaqueous liquid electrolytes for lithium-based rechargeable batteries, *Chem. Rev.*, 2004, **104**, 4303–4417.

28 A. Bottino, G. Capannelli, S. Munari and A. Turturro, Solubility parameters of poly(vinylidene fluoride), *J. Polym. Sci., Part B: Polym. Phys.*, 1988, **26**, 785–794.

29 Y. Sun, C. J. Radke, B. D. McCloskey and J. M. Prausnitz, Wetting Behavior of Four Polar Organic Solvents Containing One of Three Lithium Salts on a Lithium-Ion-Battery Separator, *J. Colloid Interface Sci.*, 2018, **529**, 582–587, DOI: [10.1016/j.jcis.2018.06.044](https://doi.org/10.1016/j.jcis.2018.06.044).

30 A. Davoodabadi, J. Li, Y. Liang, D. L. Wood, T. J. Singler and C. Jin, Analysis of Electrolyte Imbibition through Lithium-Ion Battery Electrodes, *J. Power Sources*, 2019, **424**, 193–203, DOI: [10.1016/j.jpowsour.2019.03.115](https://doi.org/10.1016/j.jpowsour.2019.03.115).

31 W. S. Chiang, J. H. Chen and Y. Liu, Investigation of Porous Materials with Large Surface Heterogeneity Using the Generalized Porod's Scattering Law Method, *Phys. Rev. E*, 2019, **99**(4), 042801, DOI: [10.1103/PhysRevE.99.042801](https://doi.org/10.1103/PhysRevE.99.042801).

32 W. S. Chiang, D. Georgi, T. Yildirim, J. H. Chen and Y. Liu, A Non-Invasive Method to Directly Quantify Surface Heterogeneity of Porous Materials, *Nat. Commun.*, 2018, **9**(1), 784, DOI: [10.1038/s41467-018-03151-w](https://doi.org/10.1038/s41467-018-03151-w).

33 Z. Zhang, T. Zeng, Y. Lai, M. Jia and J. Li, A Comparative Study of Different Binders and Their Effects on Electrochemical Properties of LiMn_2O_4 Cathode in Lithium Ion Batteries, *J. Power Sources*, 2014, **247**, 1–8, DOI: [10.1016/j.jpowsour.2013.08.051](https://doi.org/10.1016/j.jpowsour.2013.08.051).

34 H. B. Stuhrmann and R. G. Kirste, Elimination der intrapartikulären Untergrundstreuung bei der Röntgenkleinwinkelstreuung an kompakten Teilchen. II, *Zeitschrift für Physikalische Chemie*, 1967, **56**, 334–337.

35 T. M. M. Heenan, *et al.*, Identifying the Origins of Microstructural Defects Such as Cracking within Ni-Rich NMC811 Cathode Particles for Lithium-Ion Batteries, *Adv. Energy Mater.*, 2020, **10**, 2002655.

36 J. Saunier, F. Alloin, J. Y. Sanchez and B. Barrière, Plasticized microporous poly(vinylidene fluoride) separators for lithium-ion batteries. II. Poly(vinylidene fluoride) dense membrane swelling behavior in a liquid electrolyte—characterization of the swelling kinetics, *J. Polym. Sci., Part B: Polym. Phys.*, 2004, **42**, 544–552.

37 J. B. Hipp, J. J. Richards and N. J. Wagner, Direct measurements of the microstructural origin of shear-thinning in carbon black suspensions, *J. Rheol. (NY)*, 2021, **65**, 145–157.

38 J. B. Hipp, J. J. Richards and N. J. Wagner, Structure-property relationships of sheared carbon black suspensions determined by simultaneous rheological and neutron scattering measurements, *J. Rheol. (NY)*, 2019, **63**, 423–436.

39 J. J. Richards, J. B. Hipp, J. K. Riley, N. J. Wagner and P. D. Butler, Clustering and Percolation in Suspensions of Carbon Black, *Langmuir*, 2017, **33**, 12260–12266.

40 W. Haselrieder, S. Ivanov, D. K. Christen, H. Bockholt and A. Kwade, Impact of the Calendering Process on the Interfacial Structure and the Related Electrochemical Performance of Secondary Lithium-Ion Batteries, *ECS Trans.*, 2013, **50**, 59–70.

41 A. Diener, S. Ivanov, W. Haselrieder and A. Kwade, Evaluation of Deformation Behavior and Fast Elastic Recovery of Lithium-Ion Battery Cathodes via Direct Roll-Gap Detection During Calendering, *Energy Technol.*, 2022, **10**(4), 2101033, DOI: [10.1002/ente.202101033](https://doi.org/10.1002/ente.202101033).

42 C. Schilcher, C. Meyer and A. Kwade, Structural and Electrochemical Properties of Calendered Lithium Manganese Oxide Cathodes, *Energy Technol.*, 2016, **4**(12), 1604–1610, DOI: [10.1002/ente.201600130](https://doi.org/10.1002/ente.201600130).

43 H. Zheng, L. Tan, G. Liu, X. Song and V. S. Battaglia, Calendering Effects on the Physical and Electrochemical Properties of $\text{Li}[\text{Ni}_{1/3}\text{Mn}_{1/3}\text{Co}_{1/3}]\text{O}_2$ Cathode, *J. Power Sources*, 2012, **208**, 52–57, DOI: [10.1016/j.jpowsour.2012.02.001](https://doi.org/10.1016/j.jpowsour.2012.02.001).

44 M. Nikpour, N. Barrett, Z. Hillman, A. I. Thompson, B. A. Mazzeo and D. R. Wheeler, A Model for Investigating Sources of Li-Ion Battery Electrode Heterogeneity: Part I. Electrode Drying and Calendering Processes, *J. Electrochem. Soc.*, 2021, **168**(6), 060547, DOI: [10.1149/1945-7111/ac0bf1](https://doi.org/10.1149/1945-7111/ac0bf1).

45 E. N. Primo, M. Chouchane, M. Touzin, P. Vazquez and A. A. Franco, Understanding the calendering processability of $\text{Li}(\text{Ni}_{0.33}\text{Mn}_{0.33}\text{Co}_{0.33})\text{O}_2$ -based cathodes, *J. Power Sources*, 2021, **488**, 229361.

46 T. Beuse, M. Fingerle, C. Wagner, M. Winter and M. Börner, Comprehensive insights into the porosity of lithium-ion battery electrodes: A comparative study on positive electrodes based on $\text{LiNi}_{0.6}\text{Mn}_{0.2}\text{Co}_{0.2}\text{O}_2$ (NMC622), *Batteries*, 2021, **7**, 70.

47 C. Meyer, H. Bockholt, W. Haselrieder and A. Kwade, Characterization of the Calendering Process for Compaction of Electrodes for Lithium-Ion Batteries, *J. Mater. Process. Technol.*, 2017, **249**, 172–178, DOI: [10.1016/j.jmatprotec.2017.05.031](https://doi.org/10.1016/j.jmatprotec.2017.05.031).

48 A. C. Ngandjou, *et al.*, Investigating electrode calendering and its impact on electrochemical performance by means of a new discrete element method model: Towards a digital twin of Li-Ion battery manufacturing, *J. Power Sources*, 2021, **485**, 229320.

49 Q. Liu and J. J. Richards, Rheo-electric measurements of carbon black suspensions containing polyvinylidene difluoride in N-methyl-2-pyrrolidone, *J. Rheol. (NY)*, 2023, **67**, 647–659.

50 J. J. Richards, P. Z. Ramos and Q. Liu, A Review of the Shear Rheology of Carbon Black Suspensions, *Front. Phys.*, 2023, **11**, DOI: [10.3389/fphy.2023.1245847](https://doi.org/10.3389/fphy.2023.1245847).

51 S. Komini Babu, A. I. Mohamed, J. F. Whitacre and S. Litster, Multiple Imaging Mode X-Ray Computed Tomography for Distinguishing Active and Inactive Phases in Lithium-Ion Battery Cathodes, *J. Power Sources*, 2015, **283**, 314–319, DOI: [10.1016/j.jpowsour.2015.02.086](https://doi.org/10.1016/j.jpowsour.2015.02.086).

52 S. Oswald, *et al.*, Novel Method for Monitoring the Electrochemical Capacitance by In Situ Impedance Spectroscopy as Indicator for Particle Cracking of Nickel-



Rich NCMs: Part I. Theory and Validation, *J. Electrochem. Soc.*, 2020, **167**, 100511.

53 Y. H. Liu, W. C. Chen, C. H. Hsueh and C. L. Hsu, Elucidating the Function of Modified Carbon Blacks in High-Voltage Lithium-Ion Batteries: Impact on Electrolyte Decomposition, *Mater. Today Chem.*, 2022, **25**, 100934, DOI: [10.1016/j.mtchem.2022.100934](https://doi.org/10.1016/j.mtchem.2022.100934).

54 H. B. Lin, *et al.*, Surface natures of conductive carbon materials and their contributions to charge/discharge performance of cathodes for lithium ion batteries, *J. Power Sources*, 2015, **287**, 276–282.

55 J. Zheng, *et al.*, Surface and structural stabilities of carbon additives in high voltage lithium ion batteries, *J. Power Sources*, 2013, **227**, 211–217.

56 J. Syzdek, M. Marcinek and R. Kostecki, Electrochemical activity of carbon blacks in LiPF6-based organic electrolytes, *J. Power Sources*, 2014, **245**, 739–744.

57 R. Younesi, *et al.*, Analysis of the Interphase on Carbon Black Formed in High Voltage Batteries, *J. Electrochem. Soc.*, 2015, **162**, A1289–A1296.

58 S. Liu, X. Zeng, D. Liu, S. Wang, L. Zhang, R. Zhao, F. Kang and B. Li, Understanding the Conductive Carbon Additive on Electrode/Electrolyte Interface Formation in Lithium-Ion Batteries via in Situ Scanning Electrochemical Microscopy, *Front. Chem.*, 2020, **8**, DOI: [10.3389/fchem.2020.00114](https://doi.org/10.3389/fchem.2020.00114).

59 E. N. Primo, M. Chouchane, M. Touzin, P. Vazquez and A. A. Franco, Understanding the calendering processability of $\text{Li}(\text{Ni}_{0.33}\text{Mn}_{0.33}\text{Co}_{0.33})\text{O}_2$ -based cathodes, *J. Power Sources*, 2021, **488**, 229361.

60 W. T. Heller, M. Cuneo, L. Debeer-Schmitt, C. Do, L. He, L. Heroux, K. Littrell, S. V. Pingali, S. Qian, C. Stanley, V. S. Urban, B. Wu and W. Bras, The Suite of Small-Angle Neutron Scattering Instruments at Oak Ridge National Laboratory, *J. Appl. Cryst.*, 2018, **51**(2), 242–248, DOI: [10.1107/S1600576718001231](https://doi.org/10.1107/S1600576718001231), urn:issn:1600-5767, doi:.

61 J. K. Zhao, C. Y. Gao and D. Liu, The extended Q-range small-angle neutron scattering diffractometer at the SNS, *J. Appl. Crystallogr.*, 2010, **43**, 1068–1077.

62 W. T. Heller, *et al.*, drtsans: The data reduction toolkit for small-angle neutron scattering at Oak Ridge National Laboratory, *SoftwareX*, 2022, **19**, 101101.

